Physically-based impedance modeling of the negative electrode in All-Vanadium Redox Flow Batteries: insight into mass transport issues

M. Zago*, A. Casalegno

Politecnico di Milano, Department of Energy, Via Lambruschini 4, 20156 Milano, Italy

* *corresponding author matteo.zago@polimi.it*

Abstract

Mass transport of the electrolyte over the porous electrode is one of the most critical issues hindering Vanadium Redox Flow Battery commercialization, leading to increased overpotential at high current and limiting system power density. In this work, a 1D physically based impedance model of Vanadium Redox Flow Battery negative electrode is developed, taking into account electrochemical reactions, convection at carbon fiber, diffusion in the pores and migration and diffusion through electrode thickness. The model is validated with respect to experimental data measured in a symmetric cell hardware, which allows to keep the State of Charge constant during the measurement. The physically based approach permits to elucidate the origin of different impedance features and quantify the corresponding losses. Charge transfer resistance decreases with increasing current and is generally lower compared to the ones related to mass transport phenomena. Migration losses through the porous electrode are negligible, while convection at carbon fiber is relevant and in Nyquist plot results in a linear branch at low frequency. In presence of significant convection losses the reaction tends to concentrate close to the channel: this leads to a reduction of diffusion losses through the electrode, while diffusion process in the pores becomes more limiting.

Keywords: electrochemical impedance spectroscopy, mass transport, model, vanadium redox flow battery.

1. Introduction

Vanadium Redox Flow Battery (VRFB) is a promising technology for energy storage due to the peculiarities to separate power and energy, high efficiency and extremely long charge/discharge cycle life [1-4]. VRFB employs the same element in different oxidation states in both electrodes, avoiding the issue of permanent contamination between the two half-cell electrolytes [5]. However, the commercialization of VRFB is still hindered by some technological issues, among which low power density is one of the most important [4,6], since it directly affects stack size and system cost [7,8]. Therefore, the understanding of the main physical phenomena regulating VRFB operation and the quantification of the corresponding performance losses become crucial to reach market competitiveness.

Several works in the literature studied the influence of mass transport on VRFB operation [9-11]. In [9] the influence of reactants distributors and material properties was investigated, evidencing that at high current mass transport losses limit VRFB performance and the optimization of flow field architecture is strictly correlated to electrode morphology and operating conditions. In [10] a 3D numerical model was developed to analyze mass transport issues within a VRFB system, confirming that distribution uniformity of electrolyte through the electrode is fundamental to minimize the mass transfer overpotential. In [11] a macroscopic VRFB model was used to study the influence of flow rate, electrode permeability and thickness, highlighting that the penetration of the electrolyte into the porous layer strongly affects system power density. However, the quantification of the performance losses associated to the different mass transport phenomena simultaneously occurring in VRFB systems has not be extensively studied.

Electrochemical Impedance Spectroscopy (EIS) is the most common *in-situ* technique to measure system internal losses [12]. It consists in measuring the linear response of an electrochemical system perturbed in steady state with a small AC current signal over a wide

range of frequencies and in measuring the voltage response. The EIS permits to separate physical phenomena with different relaxation frequencies [13]. Despite its potentialities, the interpretation of experimental data is very difficult and usually it is carried out by means of equivalent circuit method (ECM). Even though simple and fast, the ECM is not reliable and mainly provides qualitative information [14].

An alternative approach is represented by physically based impedance modelling, which is not a trivial task, but provides more quantitative information. The modeling of the physical process occurring in the system during EIS measurement leads to model results independent of the choice of a suitable equivalent electric circuit [15-17]. In the literature many works regarding physical based modeling of fuel cells can be found [15-20]. In [18], one of the first numerical models for polymer electrolyte fuel cell cathode impedance was developed: the first impedance loop is attributed to the effective charge transfer and double layer charging, while the second one to the mass transport limitations. In [19,20], an extensive physically based model activity on solid oxide fuel cell was carried out: the detailed elementary kinetic electrochemistry and diffusion processes allow the assignment of the origin of impedance features with high accuracy.

Up to our knowledge, limited effort has been dedicated to the interpretation of impedance in VRFB systems. In [21,22] a simple equivalent electric circuit was used to extract the electron transfer constant for rough and also porous structures. In [23] the impedance of VRFB negative electrode was analyzed with a macrohomogeneous porous electrodes model, derived from a transmission line equivalent circuit in which charge transfer and finite diffusion are the limiting processes [24].

This work proposes a 1D physical-based impedance model of VRFB negative electrode, including electrochemical reactions, convection at carbon fiber, diffusion in the pores and migration and diffusion through electrode thickness. The model is validated with respect to

experimental data measured in a symmetric cell hardware, addressing the origin of different impedance features and providing a quantitative interpretation of the measurements. The work is organized as follows. In section 2 the experimental methodology is reported, subsequently, in section 3, the DC and AC model development is described. Then, in section 4, the experimental and model results are discussed and the origin of different impedance features are illustrated. Finally some conclusions are given in section 5.

2. Experimental

A detailed description of the experimental setup and impedance measurements is reported in [25,26][1]. The symmetric cell configuration was adopted [23,27], in which the negative electrolyte, consisting of water, sulfuric acid (i.e., H^+, HSO_4^- and SO_4^{2-}) and charged Vanadium ions V^{2+} and V^{3+}, is oxidized at one electrode:

$$V^{2+} \rightarrow V^{3+} + e^- \quad (1)$$

and reduced at the other electrode:

$$V^{3+} + e^- \rightarrow V^{2+} \quad (2)$$

This setup permits to keep 50% SOC during the experiments [25]. Moreover a pulse dampener, consisting of a sealed bottle with two ports [25], was adopted, permitting the measurement of low frequency (<1 Hz) impedance at high flow rates, such as 30 ml min^{-1}.

The cell was 5 cm^2 active area, fed with a single-channel serpentine flow field. The membrane was Nafion® 117 and electrode material was SGL 10 AA carbon paper (nominal thickness of ~410 μm, compressed to 300 μm). The cell temperature is maintained at 30°C.

Cell impedance was measured under potentiostatic control and the amplitude of the sinusoidal signal was 5 mV [25]. The frequency range was included between 50 kHz and 20

[1] The experimental data reported in this work has been provided by the Electrochemical Energy Storage and Conversion Laboratory of The University of Tennessee, Knoxville (USA).

mHz with a logarithmic distribution. Different electrolyte flow rates and Vanadium concentrations were tested to highlight the effect of mass transport phenomena in determining VRFB impedance. The investigated operating conditions are reported in Table 1.

3. Model

3.1 DC model Development

Figure 1A[2] reports the scheme of the VRFB half-cell undergoing V^{2+} oxidation. Flow field serves to distribute the electrolyte over the electrode surface and it is transported through the carbon structure mainly by:

- Convection, whose predominant component is in y-direction [11], coherently with the flow in the channel; moreover the difference pressure between consecutive channel induces by-bass flow under the rib [9], that is important to support high current densities, such as 0.25 A cm^{-2} [9].
- Diffusion and migration, whose predominant component is in x-direction due to the flow-field reactants distribution, that in the porous electrode limits their contribution in the y-direction.
- Diffusion from the bulk electrolyte to the carbon interface, where electrochemical reactions take place [28].

As reported in [29], the current distribution in VRFB systems is not uniform and the observed distribution is influenced by local electrolyte velocity in the porous electrode, electrolyte concentration and electrode properties, such as wettability and porosity. Also in [9], thanks to thermal visualization technique, it was possible to highlight that certain zones under the rib of two consecutive channels experience higher velocities, leading to difference in local operation over the active area. The simulation of the above mentioned local mass transport effects can

[2] The proportion between different cell layers is not maintained for the sake of readability.

be implemented only with the aid of computational fluid dynamics (CFD) in a 3D domain, but the main drawback is that it requires high computational cost and the coupling of CFD approach with impedance spectroscopy simulation has not been investigated yet in the literature.

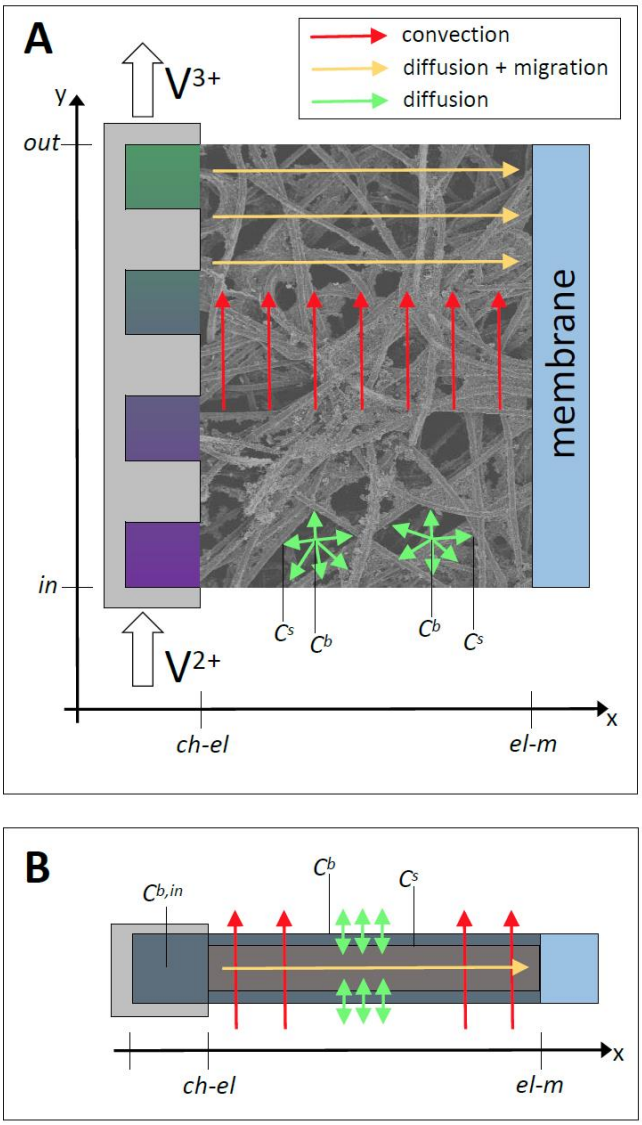

Figure 1 - A) VRFB mass transport phenomena within the porous electrode; B) 1D model domain.

Moreover, the not uniform morphology of VRFB electrodes and the relative uncertainty in the quantification of their properties, along with the lack in the literature of local impedance measurements, do not justify the necessity to develop a complex model, which is out of the scope of this work. The aim of the present analysis is to address mass transport issues

occurring in the system to a specific impedance feature. For these reasons, the simplified model domain reported in Figure 1B is adopted: the 1D assumption is reasonable considering the cell active area of 5 cm^2 and the high stoichiometry of the experiments (Table 1), which limit the gradients along the channel. In the following the main governing equations and assumptions are reported for each components.

3.1.1 Electrode

The conservation of mass for each charged species is defined using the following equations:

$$\frac{\partial N_{V^{2+}}}{\partial x} + \varepsilon_{el} \cdot \frac{\partial C^b_{V^{2+}}}{\partial t} = \frac{i_v}{F} \qquad \frac{\partial N_{V^{3+}}}{\partial x} + \varepsilon_{el} \cdot \frac{\partial C^b_{V^{3+}}}{\partial t} = -\frac{i_v}{F}$$
$$\frac{\partial N_{HSO_4^-}}{\partial x} + \varepsilon_{el} \cdot \frac{\partial C^b_{HSO_4^-}}{\partial t} = 0 \qquad \frac{\partial N_{H^+}}{\partial x} + \varepsilon_{el} \cdot \frac{\partial C^b_{H^+}}{\partial t} = 0 \tag{3}$$

where i_v is the volumetric reaction current density and the dissociation of HSO_4^- and H^+ is neglected. Equations (3) apply to all the charged species except SO_4^{2-}, which is calculated from the electro-neutrality condition, as reported in [28].

$$\sum_i z_i \cdot C_i^b = 0 \tag{4}$$

The flux of each charged species ($V^{2+}, V^{3+}, HSO_4^-, H^+, SO_4^{2-}$) is governed by Nernst-Plank equation:

$$N_i = -D_i^{eff} \cdot \frac{\partial C_i^b}{\partial x} - z_i \cdot C_i^b \cdot \frac{F \cdot D_i^{eff}}{R \cdot T} \cdot \frac{\partial \phi_l}{\partial x} \tag{5}$$

Multiplying Eq. (5) for each species by the z_i/D_i^{eff} and making the sum, it is possible to obtain an ordinary differential equation for liquid phase potential, which substitutes the Nernst-Plank equation for SO_4^{2-} in the final resolution system:

$$\frac{\partial \phi_l}{\partial x} = -\frac{R \cdot T}{F} \cdot \frac{\frac{z_{V^{2+}}}{D^{eff}_{V^{2+}}} \cdot N_{V^{2+}} + \frac{z_{V^{3+}}}{D^{eff}_{V^{3+}}} \cdot N_{V^{3+}} + \frac{z_{HSO_4^-}}{D^{eff}_{HSO_4^-}} \cdot N_{HSO_4^-} + \frac{z_{H^+}}{D^{eff}_{H^+}} \cdot N_{H^+} + \frac{z_{SO_4^{2-}}}{D^{eff}_{SO_4^{2-}}} \cdot N_{SO_4^{2-}}}{(z^2_{V^{2+}} \cdot C^b_{V^{2+}} + z^2_{V^{3+}} \cdot C^b_{V^{3+}} + z^2_{HSO_4^-} \cdot C^b_{HSO_4^-} + z^2_{H^+} \cdot C^b_{H^+} + z^2_{SO_4^{2-}} \cdot C^b_{SO_4^{2-}})} \tag{6}$$

where $C^b_{SO_4^{2-}}$ is calculated from Eq. (4), while $N_{SO_4^{2-}}$ is obtained from:

$$i_l = \sum_i z_i \cdot F \cdot N_i \tag{7}$$

Considering that the solid phase current is opposite to the liquid phase one [30], the variation of solid phase potential turns out to be:

$$\frac{\partial \phi_s}{\partial x} = \frac{i_l}{\sigma_s} \tag{8}$$

The variation of i_l through electrode thickness is equal to the volumetric reaction current density i_v, resulting in:

$$\frac{\partial i_l}{\partial x} - C_{dl} \cdot \frac{\partial \eta}{\partial t} = a \cdot F \cdot k^- \cdot \left\{ C^s_{V^{2+}} \cdot \exp\left(\frac{\alpha \cdot F \cdot \eta}{R \cdot T} \right) - C^s_{V^{3+}} \cdot \exp\left(\frac{-(1-\alpha) \cdot F \cdot \eta}{R \cdot T} \right) \right\} \tag{9}$$

where C_{dl} is the double layer capacitance and η is defined coherently with [31] as:

$$\eta = \phi_s - \phi_l - E_0 \tag{10}$$

with E_0 defined as the standard equilibrium potential.

The $C^s_{V^{2+}}$ and $C^s_{V^{3+}}$ are the Vanadium concentrations to the surface of the carbon fiber, where electrochemical reactions occur, and can be derived solving the following equations:

$$\begin{aligned} \frac{F \cdot D_{V^{2+}}}{r_p} \cdot \left(C^b_{V^{2+}} - C^s_{V^{2+}} \right) &= F \cdot k^- \cdot \left\{ C^s_{V^{2+}} \cdot \exp\left[\frac{\alpha \cdot F \cdot \eta}{R \cdot T} \right] - C^s_{V^{3+}} \cdot \exp\left[\frac{-(1-\alpha) \cdot F \cdot \eta}{R \cdot T} \right] \right\} \\ \frac{F \cdot D_{V^{3+}}}{r_p} \cdot \left(C^b_{V^{3+}} - C^s_{V^{3+}} \right) &= -F \cdot k^- \cdot \left\{ C^s_{V^{2+}} \cdot \exp\left[\frac{\alpha \cdot F \cdot \eta}{R \cdot T} \right] - C^s_{V^{3+}} \cdot \exp\left[\frac{-(1-\alpha) \cdot F \cdot \eta}{R \cdot T} \right] \right\} \end{aligned} \tag{11}$$

in which the mass transport rate by means of diffusion in the pores of the electrode equals the rate of local electrochemical reaction [32]. Assuming that the diffusivity of V^{2+} is equal to the V^{3+} one, the Vanadium concentrations at the active sites can be expressed as:

$$C^s_{V^{2+}} = \frac{C^b_{V^{2+}} \cdot \frac{D}{r_p \cdot k^-} + \left(C^b_{V^{2+}} + C^b_{V^{3+}}\right) \cdot \exp\left(-\frac{(1-\alpha)\cdot F \cdot \eta}{R \cdot T}\right)}{\exp\left(\frac{\alpha \cdot F \cdot \eta}{R \cdot T}\right) + \exp\left(-\frac{(1-\alpha)\cdot F \cdot \eta}{R \cdot T}\right) + \frac{D}{r_p \cdot k^-}}$$

$$C^s_{V^{3+}} = \frac{C^s_{V^{2+}} \cdot \exp\left(\frac{\alpha \cdot F \cdot \eta}{R \cdot T}\right) - \left(C^b_{V^{2+}} - C^s_{V^{2+}}\right) \cdot \frac{D}{r_p \cdot k^-}}{\exp\left(-\frac{(1-\alpha)\cdot F \cdot \eta}{R \cdot T}\right)} \quad (12)$$

Moreover, the electrolyte bulk concentration is limited by convective mass transport at carbon fiber, which is included in the boundary conditions (Eq. (14)). Due to the complex and highly uncertain hydrodynamics inside the porous media, the value of the mass transport convective coefficient (h_{conv}) has been fitted with respect to experimental data. As reported in section 3.1, this approach does not pretend to be rigorous, but it has been carried out in order to evaluate the origin of the different impedance features. The resulting convective coefficient are subsequently compared with the ones reported in the literature [33], as described in section 4.

3.1.2 Membrane

The polymer electrolyte membrane is assumed permeable to only protons. No Vanadium ions crossover is considered since its effect on performance loss is relevant after many charge-discharge cycles [4]. Indeed the voltage loss related to proton transport across the membrane is given by Ohm's law:

$$\eta_{Ohm} = i_l \cdot l_m / \sigma_m \quad (13)$$

where l_m is membrane thickness and σ_m is the proton conductivity, which is assumed constant.

3.1.3 Numerical resolution

The 1D VRFB model is implemented in MATLAB®. The final DC system describing electrode behavior, in which time derivatives are set to zero, is composed by 11 ordinary differential equations and it is subject to the following boundary conditions:

$$i_l\big|_{ch-el} = 0 \qquad i_l\big|_{el-m} = i_{VRFB}$$

$$N_i\big|_{el-m} = 0 \qquad i = \left\{V^{2+}, V^{3+}, HSO_4^-\right\}$$

$$N_{H^+}\big|_{el-m} = i_{VRFB} / F \tag{14}$$

$$\phi_s\big|_{ch-el} = 0$$

$$C_i^b\big|_{ch-el} = C_i^{b,in} - N_i \,/ h_{conv} \qquad i = \left\{V^{2+}, V^{3+}, HSO_4^-, H^+\right\}$$

The electrode system is a two-point boundary value problem and the built in bvp5c function has been used for the numerical resolution of Equations (3)-(12). The electrolyte bulk concentration at channel-electrode interface is affected by convective flux: considering convective mass transport notions [34], due to the complexities encountered with a rigorous treatment of the hydrodynamic at carbon fiber, a simplified approach compatible with impedance simulation has been adopted. The convective flux is thus expressed as the convective mass transport coefficient multiplied by the difference between bulk concentration in the channel and bulk concentration at channel-electrode interface. The fluxes and concentrations of SO_4^{2-} are calculated by means of algebraic Eq. (4) and (7), respectively.

3.2 AC model development

After obtaining the stationary solution, the AC model of the VRFB negative electrode is obtained with the mathematical approach described in [13,14], which is based on Laplace transform and system linearization around the steady-state, coherently with the EIS linearity hypothesis.

3.2.1 Electrode

Equations (6), (9) and (12) are linearized about a steady-state value and subsequently each of the variables k_i of Equations (3)-(12) are perturbed about a steady-state value with a sufficiently low sinusoidal disturbance:

$$k_i(t) = k_i^0 + \mathrm{Re}\left\{\tilde{k}_i \cdot \exp\left(j \cdot \omega \cdot t\right)\right\} \tag{15}$$

Neglecting the terms with products of the disturbances and subtracting the steady-state equations, it is possible to obtain a system of linear equations for the complex perturbation amplitudes $\tilde{k}_i$ in the frequency domain, as reported in [14].

The steady-state unknowns in the linear equations of the DC model are substituted by the corresponding oscillating amplitudes, identified by the tilde superscript, while the time derivatives in Eq. (3) and (9) are replaced by the oscillating unknown times $j \cdot \omega$.

The linearized Equations (6), (9) and (12) become:

$$\begin{aligned}
&\frac{\partial \tilde{\phi}_l}{\partial x} = \sum_i \left.\frac{\partial \phi_l}{\partial N_i}\right|_0 \cdot \tilde{N}_i + \sum_i \left.\frac{\partial \phi_l}{\partial C_i^b}\right|_0 \cdot \tilde{N}_i \\
&\frac{\partial \tilde{i}_l}{\partial x} = \left.\frac{\partial i_v}{\partial \eta}\right|_0 \cdot \tilde{\eta} + \left.\frac{\partial i_v}{\partial C^s_{V^{2+}}}\right|_0 \cdot \tilde{C}^s_{V^{2+}} + \left.\frac{\partial i_v}{\partial C^s_{V^{3+}}}\right|_0 \cdot \tilde{C}^s_{V^{3+}} + C_{dl} \cdot j \cdot \omega \cdot \tilde{\eta} \\
&\tilde{C}^s_{V^{2+}} = \left.\frac{\partial C^s_{V^{2+}}}{\partial \eta}\right|_0 \cdot \tilde{\eta} + \left.\frac{\partial C^s_{V^{2+}}}{\partial C^b_{V^{2+}}}\right|_0 \cdot \tilde{C}^b_{V^{2+}} + \left.\frac{\partial C^s_{V^{2+}}}{\partial C^b_{V^{3+}}}\right|_0 \cdot \tilde{C}^b_{V^{3+}} \\
&\tilde{C}^s_{V^{3+}} = \left.\frac{\partial C^s_{V^{3+}}}{\partial \eta}\right|_0 \cdot \tilde{\eta} + \left.\frac{\partial C^s_{V^{3+}}}{\partial C^s_{V^{2+}}}\right|_0 \cdot \tilde{C}^s_{V^{2+}} + \left.\frac{\partial C^s_{V^{3+}}}{\partial C^b_{V^{2+}}}\right|_0 \cdot \tilde{C}^b_{V^{2+}}
\end{aligned} \tag{16}$$

The steady-state derivate in Eq. (16) are reported in the Appendix A for the sake of shortness. The AC electrode system includes the impedance features related to convection, diffusion and migration through the electrode and diffusion from the bulk of the pore to the active sites.

3.2.2 Membrane

Since membrane behavior is described by a linear equation (i.e., Ohm's law), its contribution to the impedance simply turns out in a resistance equal to the ratio between membrane thickness and the conductivity.

3.2.3 Numerical resolution

Coherently with the DC model development, the AC electrode system, composed by 11 differential equations, is solved with bvp5c function and is subject to the following boundary conditions:

$$\tilde{i}_l\big|_{ch-el} = 0 \qquad \tilde{i}_l\big|_{el-m} = \tilde{i}_{VRFB}$$

$$\tilde{N}_i\big|_{el-m} = 0 \qquad i = \left\{V^{2+}, V^{3+}, HSO_4^-\right\}$$

$$\tilde{N}_{H^+}\big|_{el-m} = \tilde{i}_{VRFB} / F \tag{17}$$

$$\tilde{\phi}_s\big|_{ch-el} = \phi_s^{EIS}$$

$$\tilde{C}_i^b\big|_{ch-el} = \tilde{N}_i \big/ h_{conv} \qquad i = \left\{V^{2+}, V^{3+}, HSO_4^-, H^+\right\}$$

in which a small amplitude perturbation of solid phase potential ϕ_s^{EIS} is imposed at electrode interface facing the channel. The electrode impedance is defined as the ration between the oscillating overpotential and current at the electrode interface facing to the membrane:

$$Z_{el} = \left.\frac{\tilde{\eta}}{\tilde{i}_l}\right|_{el-m} \tag{18}$$

Thus the impedance of the symmetric cell is given by the sum of membrane resistance and electrode impedance relative to both V^{2+} oxidation and V^{3+} reduction[3] reactions:

[3] Electrode impedance relative to oxidation ($Z_{el,ox}$) or reduction ($Z_{el,rd}$) is independently obtained by solving the electrode model with positive (oxidation) or negative (reduction) DC current.

$$Z_{cell} = Z_{el,ox} + Z_{el,rd} + R_m \quad (19)$$

4. Results discussion

4.1 *Experimental*

Figures 2 report Nyquist and Bode plot at 30 ml min^{-1} and 0.8 M. Two clear impedance features are evident: the first one, whose relaxation frequency is around 0.5 kHz, characterizes kinetic losses, while the one at low frequency, lower than 1 Hz, is usually attributed to mass transport losses [12].

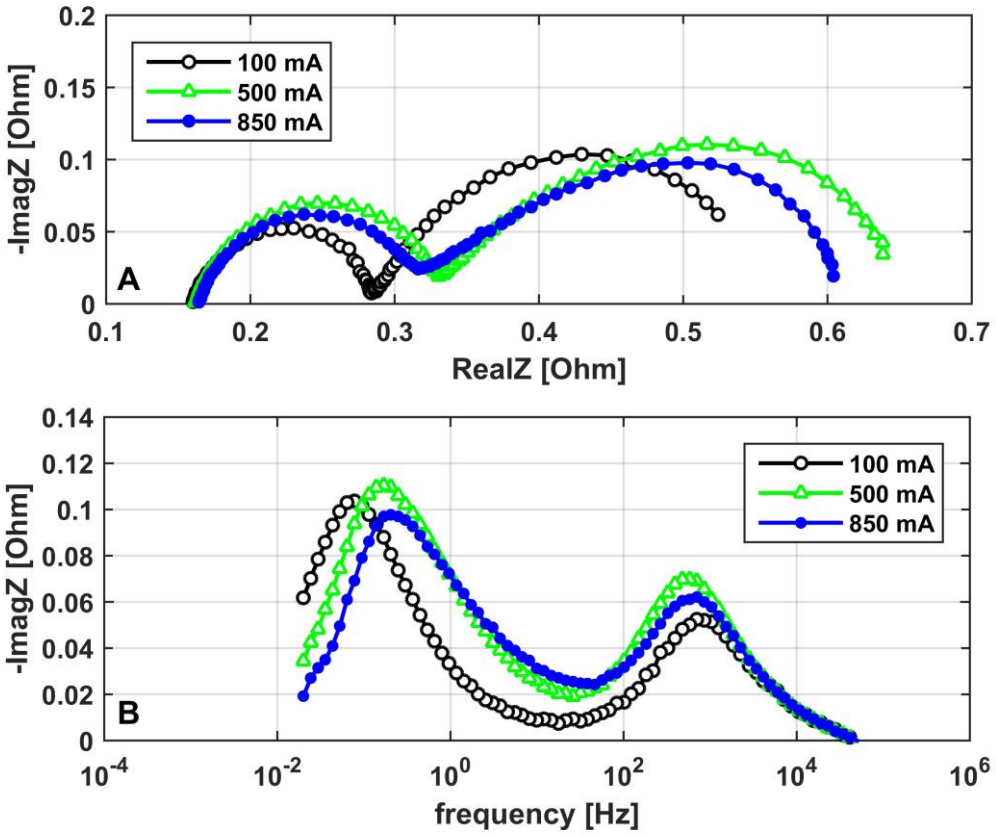

Figure 2 – Influence of current on measured impedance at 30 ml min-1 and 0.8 M: A) Nyquist plot; B) Bode plot.

It is possible to notice an unusual behavior of both impedance features: they first enlarge with increasing current and then they decrease. In the literature, it is consolidated that a pure kinetic arch decreases with increasing current [35], while a mass transport feature exhibits

the opposite trend. Moreover, the second arch presents an elongation at higher current, i.e. 850 mA.

The effect of different concentration and flow rate on impedance spectra is reported in Figure 3A and 3B, respectively. Lower Vanadium concentration and electrolyte flow rate imply an increase of both impedance features: in particular reduced concentration has a detrimental effect on the first impedance feature, while lower flow rate coupled with high current density manifests itself as an evident elongation of the second arch.

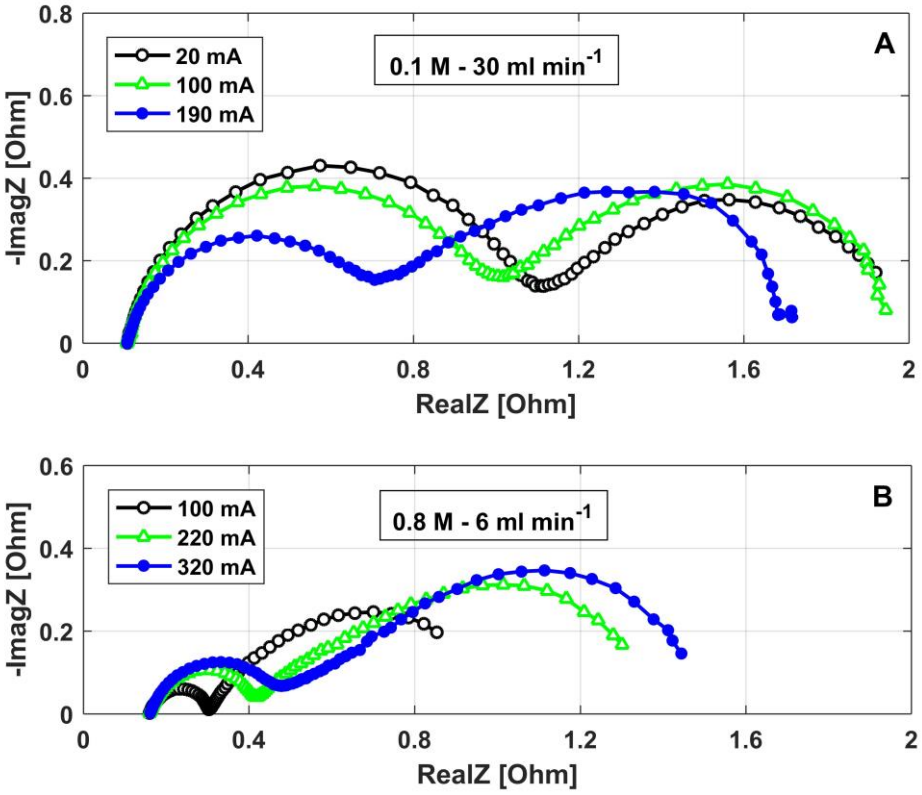

Figure 3 – Influence of current on measured Nyquist plot at: A) 30 ml min^{-1} and 0.1 M; B) 6 ml min^{-1} and 0.8 M.

Thus, physical-based modeling analysis becomes crucial to understand the origin of the above described impedance features, permitting the quantification of system internal losses.

4.2 Model

The model is validated with respect to the experimental measurements at 0.8 M and 30 ml min^{-1}. Assumed and fitted model parameters (Table 2) are consistent with those reported in the literature: the resulting transfer coefficient is close to 0.5 [23] and the rate constant is $2.24 \cdot 10^{-6}$ m s^{-1}, coherently with the values reported in [25], where this value is included between $1 \cdot 10^{-6}$ and $1.5 \cdot 10^{-6}$ m s^{-1}. The resulting convective mass transport coefficient is $1.1 \cdot 10^{-4}$ m s^{-1}. Assuming a Vanadium diffusivity of $2.4 \cdot 10^{-10}$ m^2 s^{-1} [28] and an average carbon fiber diameter of 8 μm, such a value can be obtained from the correlation [33]:

$$Sh = 7 \cdot \mathrm{Re}^{0.4} \tag{20}$$

that returns a convective mass transport coefficient equal to $1.1 \cdot 10^{-4}$ m s^{-1} for *Re* close to 0.15, corresponding to an average electrolyte velocity at the carbon fiber of nearly 0.05 m s^{-1}. At 30 ml min^{-1} the velocity in the channel is 0.5 m s^{-1} and considering that the velocity in the porous electrode is one order of magnitude lower, as reported in [11], the resulting mass transport convective coefficient is physically consistent. Instead the value of V^{2+}/V^{3+} effective diffusivity is 2 times higher than the one reported in [23]: considering that the developed model is reduced to 1D and the description of fluid dynamics through porous electrode is simplified, the high value is considered acceptable.

Figure 4 reports a comparison between simulated and measured Nyquist plots at different operating current. The model is able to reproduce experiments with acceptable accuracy and there is good agreement between simulated and measured relaxation frequencies: therefore all the main physical phenomena are correctly described.

The developed model replicates the increase and subsequent decrease of the first impedance arch with increasing current: this aspect is also highlighted in Figure B.1, where other two operating current are included to increase model consistency with experimental data. Instead the model slightly overestimates the second impedance arch: considering the 1D model

domain and the simplified approach for the hydrodynamic at carbon fiber, the agreement with the data is acceptable.

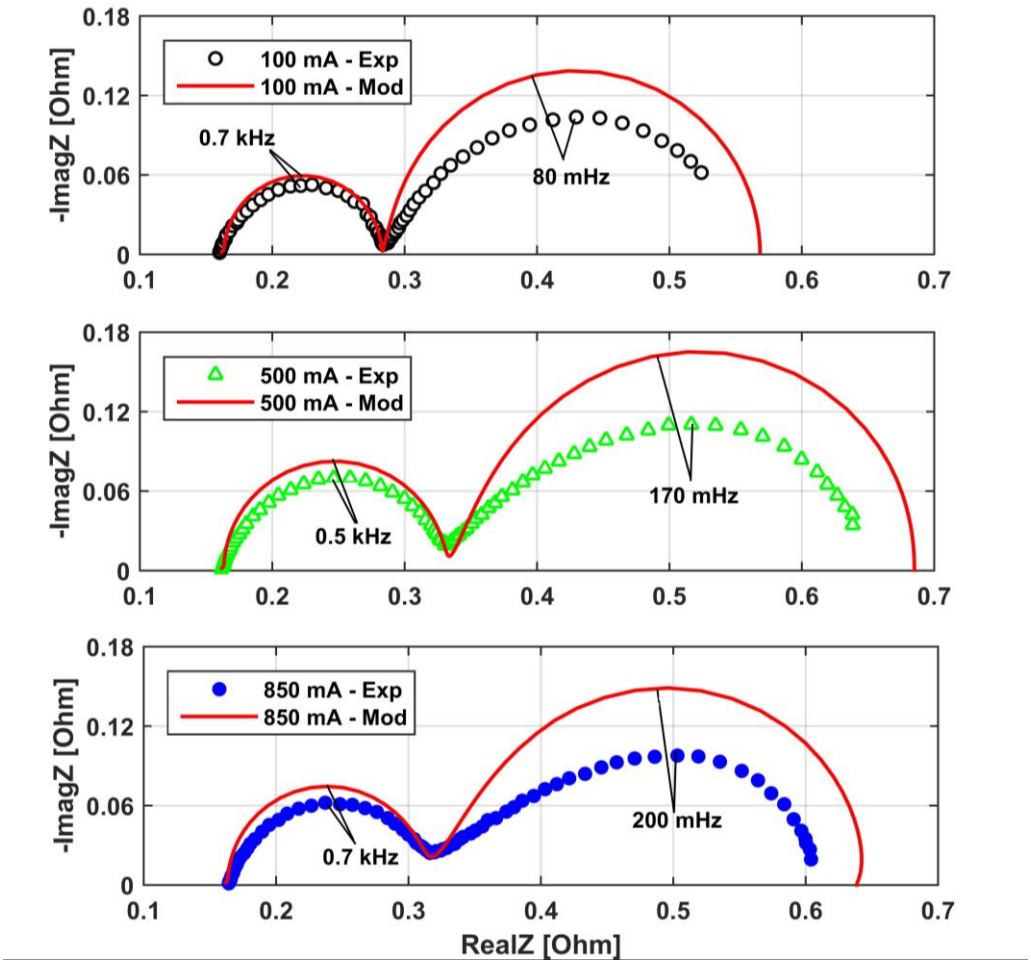

Figure 4 – Comparison between simulated and measured Nyquist plot at 30 ml min^{-1} and 0.8 M.

An overestimation of the second arch, which is influenced by real geometries and local operating conditions, is frequently encountered in physically based impedance models found in the literature [17, 36]. Moreover, the developed model reproduces impedance spectra acquired at five different operating currents with the same set of physical parameters, reducing the accuracy of data fit, but increasing the validity and reliability of the results. However, the model qualitatively reproduces the shape of the second arch: ideal semicircle at low current (100 mA) and elongated at high current (850 mA). Moreover, the increase and subsequent decrease of the second arch with increasing current, described in section 4.1, is captured by the developed model: at 500 mA both simulations and data present an enlarged

second arch. Since model results do not depend on the adopted equivalent electric circuit, the physically-based approach allows the direct assessment of the origin of impedance. As proposed in [36], the model is thus reduced by simplifying the mass transport phenomena in both DC and AC models. The effect of migration is obtained by substituting the Nernst-Plank equation, Eq. (5), with the Fick's law of diffusion; while the loss related to convection at carbon fiber is removed setting in the DC model the bulk concentration at channel-electrode interface equal to the one in the channel and imposing in the AC model the corresponding oscillating concentration equal to zero. The contribution of diffusion in the pore of the electrode is eliminated setting the surface concentration at the carbon fiber equal to the bulk concentration in the electrolyte. At last, imposing the Vanadium concentration through the electrode constant and equal to the one at channel inlet, it is possible to eliminate from the system any mass transport phenomena, highlighting the pure charge transfer loss. The model reduction approach permits to evaluate the effect of one specific physical process on impedance behavior and quantify the corresponding loss: an example is reported in Figure 5, where migration has been neglected for the sake of clarity, since its contribution is negligible.

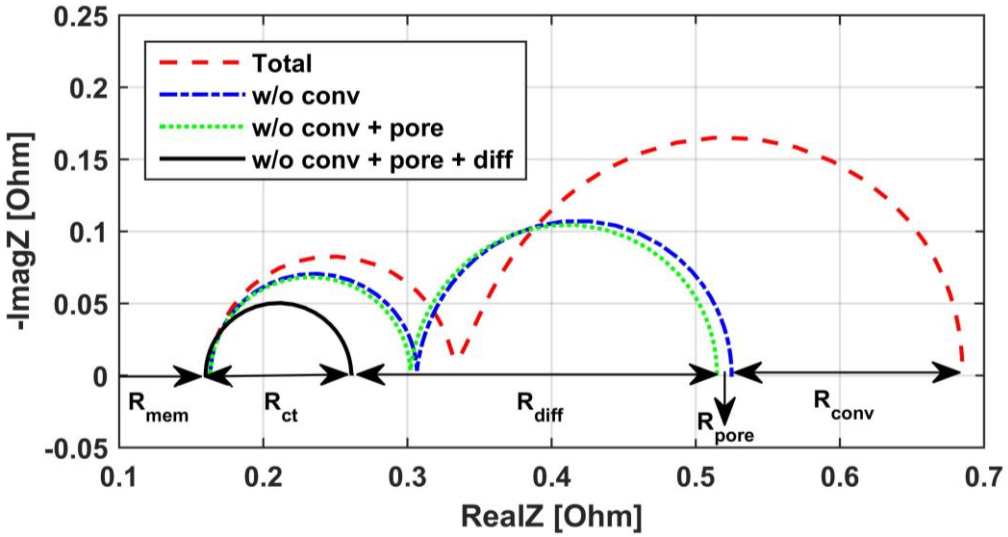

Figure 5 – Effect of different physical phenomena on Nyquist plot at 500 mA, 30 ml min^{-1}, 0.8 M and definition of the corresponding resistances.

From Figure 5 it is possible to evidence that convection affects both impedance features and is also responsible for the linear part in the low frequency region: in fact without convection the second arch is no more elongated and becomes an ideal semicircle. Diffusion from the bulk of the pore to the active surface has a minor effect and mainly influences the second arch, while diffusion through the electrode affects both impedance features, but its effect is predominant in the low frequency region, as expected. Instead, without any mass transport issues within the electrode only charge transfer is highlighted and it turns out to be an ideal semicircle at high frequency.

As reported in Figure 5, by making the difference between the total resistances[4] with and without one specific physical phenomenon, it is possible to define its corresponding resistance. In this work the resistances associated to ohmic loss in the membrane (R_{mem}), to charge transfer reaction (R_{ct}), to convection at carbon fiber (R_{conv}), to diffusion in electrode pores (R_{pore}) and to diffusion and migration through electrode thickness (R_{diff} *and* R_{mig}) are defined and evaluated. The resulting values at 0.8 M and 30 ml min^{-1} for different current are reported in Figure 6.

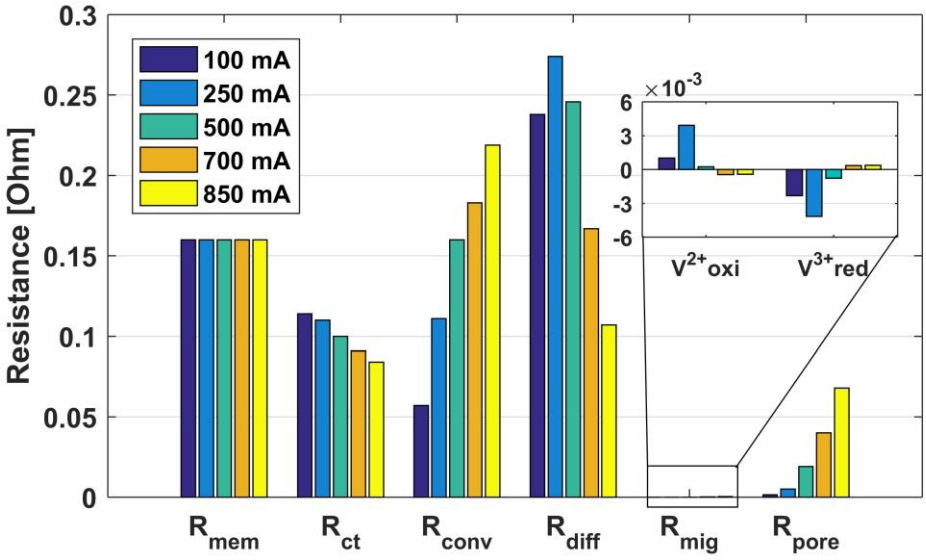

Figure 6 – Resistances associated to different physical phenomena at 0.8 M and 30 ml min^{-1} in function of operating current.

[4] The total resistance is defined as the x-axis intercept at zero frequency.

From the analysis of Figure 6 it is possible to notice that the magnitude of R_{mem} is not negligible and its value keeps constant with the current, coherently with model assumption in Eq. (13). The charge transfer resistance decreases with increasing current and since it is defined as the ratio of derivative of overpotential and derivative of current at fixed concentration [37], this result is consistent with the logarithmic relation between overpotential and current, expressed by Butler-Volmer kinetic [31]. The resulting values are generally lower compared to the ones related to mass transport issues, evidencing that in VRFB the mass transport losses hinder system performance.

The resistance associated to migration through the porous electrode is negligible. Interestingly, it is both positive and negative and at fixed current it presents opposite values between V^{2+} oxidation and V^{3+} reduction: this is induced by the different profiles of liquid phase potential through porous electrode during electrolyte oxidation and reduction. As reported in Eq. (5), negative derivative of liquid phase potential represents an additional driving force to mass transport of the electrolyte through the electrode: in this case eliminating migration from model equations leads to a negative resistance. Mass transport resistance induced by diffusion from the bulk of the pore to the active area presents low value: it increases with the current since it is proportional to the rate of local electrochemical reaction in the pore, as reported in Eq. (11). Higher values of operating current would imply a dramatic increase of such resistance. The losses related to both convection at the carbon fiber and diffusion through the porous electrode result in significant resistances: the former increases with the current since it is proportional to the flux of electrolyte, the latter increase and then decrease with the current. This result is coherent with the experimental data reported in Figure 2, in which the low frequency impedance feature exhibits a reduction at high current.

The origin of such a behavior is explained in Figure 7, in which the ionic current through the electrode thickness during V^{2+} oxidation is reported with and without the losses associated to convection at carbon fiber.

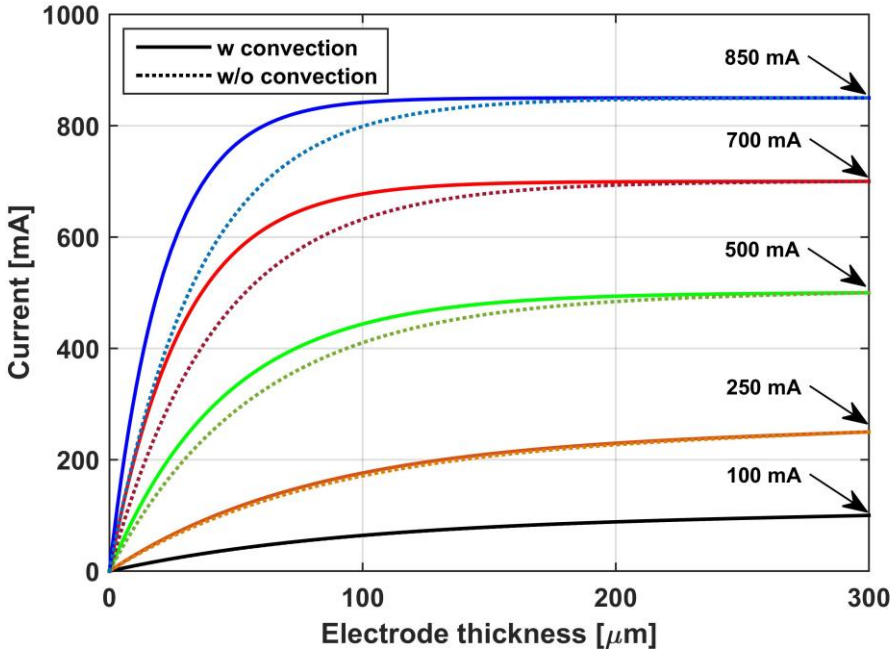

Figure 7 – Ionic current distribution through electrode thickness during V^{2+} oxidation with and without losses related to convection at the carbon fiber (zero electrode thickness at channel interface).

The presence of convection resistance lowers the V^{2+} concentration close to the electrode carbon fiber, making at high current the diffusion process through the electrode more limiting and concentrating the reaction close to the channel. As reported in Figure C.1, this implies a decrease of the characteristic length of diffusion at high current, leading to a reduction of diffusion resistance, coherently with the experimental observations of Figure 2. At 100 and 250 mA the influence of convection on current profiles is negligible, resulting in augmented diffusion resistance with increasing current, as expected. The more the reaction is concentrated in the electrode, the more the loss due to diffusion in the pores becomes relevant, as confirmed in Figure 6, in which the corresponding resistance exhibits a clear non linear behavior with the increasing current.

Keeping the same model parameters, except for the membrane conductivity and the convective mass transport coefficient, whose value has been fitted with respect to the measurements at 6 ml min^{-1} (Figure 3B), the model is able to qualitatively reproduce the effect of different concentration and flow rate on impedance spectra.

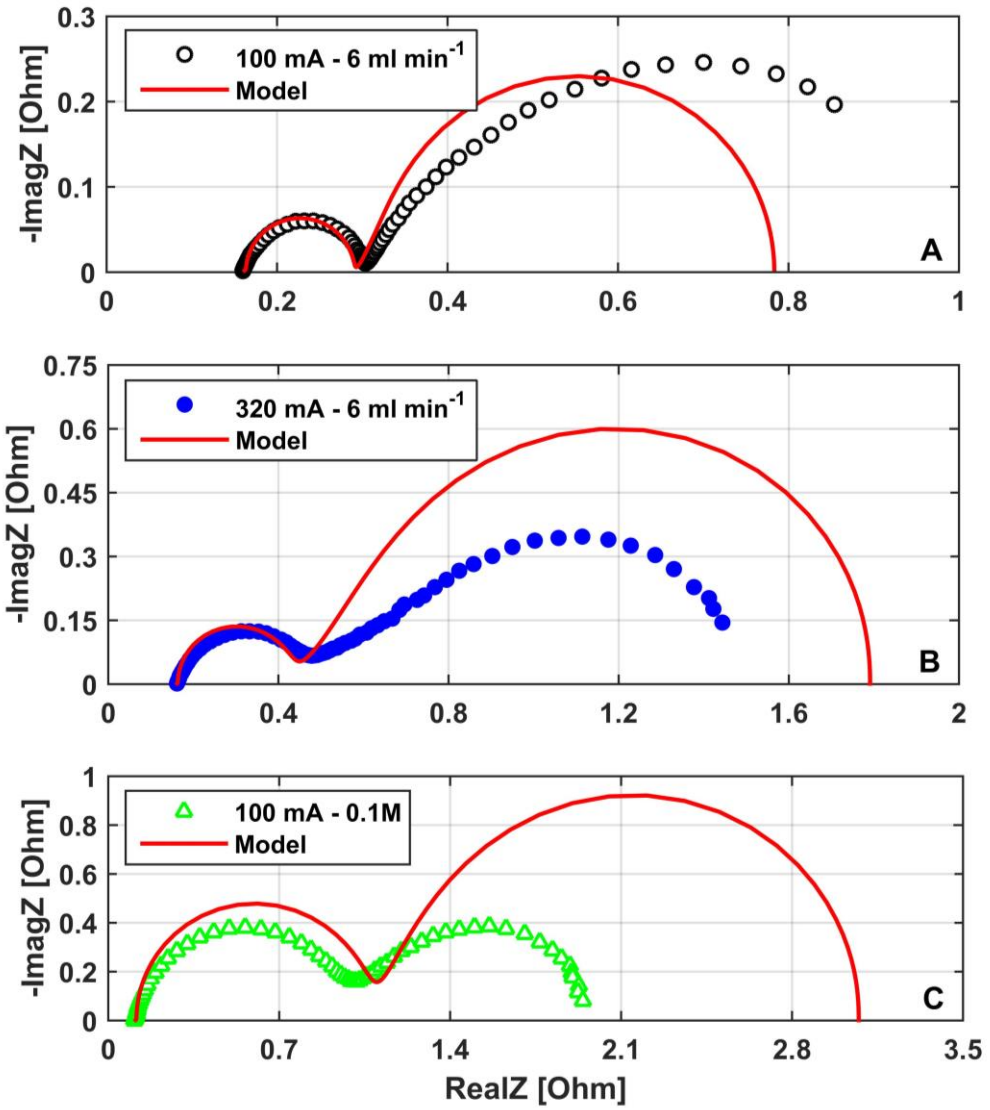

Figure 8 – Comparison between simulated and measured Nyquist plot at: A) 100 mA, 6 ml min^{-1}, 0.8 M; B) 320 mA, 6 ml min^{-1}, 0.8 M; C) 100 mA, 30 ml min^{-1}, 0.1 M.

The resulting convective coefficient ($2.75 \cdot 10^{-5}$ m s^{-1}, Table 2) is reasonably lower than the one obtained at the 30 ml min^{-1} and is coherent with the adopted correlation in Eq. (20). It is important to figure out that it would be possible to obtain more accurate impedance simulations by slightly changing few physical parameters, but this is out the scope of this

work. Moreover, the variation of both flow rate and concentration is relevant compared to the condition in which the model has been validated (30 ml min^{-1} and 0.8 M): the concentration is reduced by nearly 90% and the flow rate by 80%. However, the model reproduces with good accuracy the first impedance arch, while the second one is generally overestimated. In particular at 0.1 M, Figure 8.C, the extremely low Vanadium concentration could lead to heterogeneous operation and local mass transport effects, that are not included in the model. In both experimental data and model simulations, at 320 mA and 6 ml min^{-1} the linear part in the low frequency region due to convection is more evident, while lower concentration has a strong influence on both impedance features. These results strengthen the validity of the model and therefore the main physical phenomena regulating VRFB are correctly described.

Finally the effect of operating conditions on the resistances associated to the different physical phenomena at the same operating current (100 mA) is reported in Figure 9[5].

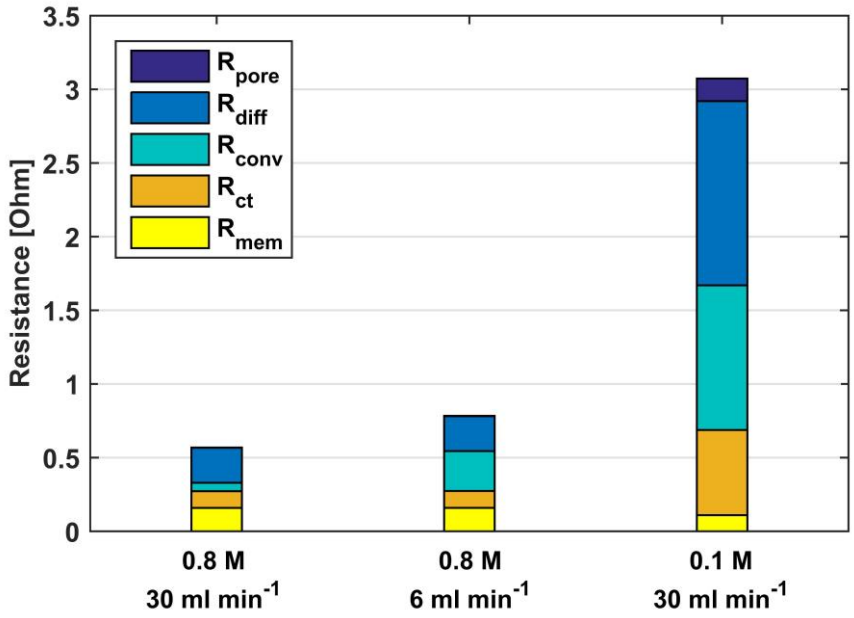

Figure 9 – Comparison between resistances associated to different physical phenomena at 100 mA in different operating conditions.

[5] Please note that the values of resistances at 0.8 M - 6 ml min^{-1} and at 0.1 M - 30 ml min^{-1} are more qualitative, since the agreement between model and experiments is worse. Migration resistance has been omitted due to its negligible contribution.

At 0.8 M, reducing the flow rate mainly affects the convective resistance, while the others keep nearly constant: this because at 100 mA the effect of convection on current profile through the electrode is negligible, as described in Figure 7. Simulations at 320 mA with different electrolyte flow rates reveal a higher increase of convective resistance, Figure D.1.A. At fixed current, the higher is the loss associated to convection at carbon fiber, the more the reaction is concentrated close to the channel, Figure D.1.B, leading to a reduction of R_{diff} and to an increase of R_{pore}, as previously explained.

At 30 ml min^{-1}, reducing the concentration has a detrimental effect on all the resistances, in particular the resistances associated to diffusion processes in the pore and through the electrode thickness increase due to the lower concentration, while the loss due to convection at carbon fiber becomes more relevant since the same concentration difference is applied to a lower bulk concentration, as reported in Eq. (14). Also charge transfer resistance enlarges because even without any mass transport losses the concentration in the active sites is set to 0.1 M, instead of 0.8 M.

From the presented physical based impedance analyses turn out that in all the investigated operating conditions mass transport issues in the porous electrode limit system performance.

5. Conclusions

This work presents the development of physically based impedance model of the negative electrode in a VRFB system. The 1D model takes into account the main mass transport issues within the porous electrode, such as diffusion processes in the pores and through the electrode, migration induced by electrolyte potential differences and convection at carbon fiber. The latter, due to the complexities and uncertainties encountered with a rigorous treatment of the hydrodynamic at carbon fiber, is simplified introducing a convective mass transport coefficient. The model has been calibrated with respect to experimental data

performed at 30 ml min^{-1} and 0.8 M at different operating currents in a symmetric cell configuration, which permits to maintain the SOC constant during the measurement. Keeping the same model parameters, validation with data recorded in different operating conditions has been performed, showing a qualitative agreement of model simulations. The main conclusions of the presented analysis are the following:

- In the investigated operating conditions VRFB impedance exhibits two distinct arches, that firstly enlarge and then decrease with increasing current. The modeling analysis highlights that mass transport losses within the electrode affect both impedance features: in particular convection results in a linear branch in the low frequency region, while low concentration has a detrimental effect on both impedance arches.
- Charge transfer process turns out to be an ideal semi-circle and the corresponding resistance decreases with increasing current: its value is generally lower compared to the ones related to mass transport issues, it is affected by electrolyte feeding concentration, but it is independent from the considered flow rate.
- The losses associated to migration through the porous electrode are negligible and the corresponding resistance is both positive and negative and at fixed current it presents opposite values between V^{2+} oxidation and V^{3+} reduction.
- The losses induced by convection at carbon fiber are relevant and proportional to the operating current, they increase with low flow rates and concentrations. When significant convection resistance is present, the reaction tends to concentrate close to the channel and this leads to a double effect. On one side the diffusion losses through the electrode diminishes, coherently with the reduction of the second impedance feature observed at high current, on the other side the diffusion process in the pores becomes more limiting and the corresponding resistance exhibits a clear non linear behavior with the increasing current.

Acknowledgement

The authors acknowledge the Electrochemical Energy Storage and Conversion Laboratory of University of Tennessee for providing the experimental data. The authors would like to thank prof. M.M. Mench, D.A. Aaron and A.M. Pezeshki for the fruitful discussions. This work has been partially funded by Fondi di Ateneo per la Ricerca di Base of Politecnico di Milano.

Appendix A

The steady-state derivative in Eq. (16) are listed below:

- liquid phase potential:

$$\left.\frac{\partial \phi_l}{\partial N_i}\right|_0 = -\frac{R\cdot T}{F}\cdot\frac{z_i}{D_i^{eff}}\cdot\frac{1}{\sum_i z_i^2\cdot C_i^b}$$

$$\left.\frac{\partial \phi_l}{\partial C_i^b}\right|_0 = \frac{R\cdot T}{F}\cdot\frac{z_i^2}{\left(\sum_i z_i^2\cdot C_i^b\right)^2}\cdot\sum_i\left(\frac{z_i}{D_i^{eff}}\cdot N_i\right) \quad \text{(A.1)}$$

- liquid phase current:

$$\left.\frac{\partial i_l}{\partial \eta}\right|_0 = a\cdot F\cdot K^-\cdot\left\{C^s_{V^{2+}}\cdot\left(\frac{\alpha\cdot F}{R\cdot T}\right)\cdot\exp\left(\frac{\alpha\cdot F\cdot\eta}{R\cdot T}\right) - C^s_{V^{3+}}\cdot\left(-\frac{(1-\alpha)\cdot F}{R\cdot T}\right)\cdot\exp\left(-\frac{(1-\alpha)\cdot F\cdot\eta}{R\cdot T}\right)\right\}$$

$$\left.\frac{\partial i_l}{\partial C^s_{V^{2+}}}\right|_0 = a\cdot F\cdot K^-\cdot\exp\left(\frac{\alpha\cdot F\cdot\eta}{R\cdot T}\right) \quad \text{(A.2)}$$

$$\left.\frac{\partial i_l}{\partial C^s_{V^{2+}}}\right|_0 = -a\cdot F\cdot K^-\cdot\exp\left(-\frac{(1-\alpha)\cdot F\cdot\eta}{R\cdot T}\right)$$

- V^{2+} surface concentration:

$$A = C^{b}_{V^{2+}} \cdot \frac{D}{r_p \cdot k^{-}} + \left(C^{b}_{V^{2+}} + C^{b}_{V^{3+}}\right) \cdot \exp\left(-\frac{(1-\alpha)\cdot F \cdot \eta}{R \cdot T}\right)$$

$$B = \exp\left(\frac{\alpha \cdot F \cdot \eta}{R \cdot T}\right) + \exp\left(-\frac{(1-\alpha)\cdot F \cdot \eta}{R \cdot T}\right) + \frac{D}{r_p \cdot k^{-}}$$

$$\frac{\partial C^{s}_{V^{2+}}}{\partial \eta} = \left\{\exp\left(-\frac{(1-\alpha)\cdot F \cdot \eta}{R \cdot T}\right) \cdot \left(\frac{-(1-\alpha)\cdot F}{R \cdot T}\right) \cdot \left(C^{b}_{V^{2+}} + C^{b}_{V^{3+}}\right) \cdot B + \right.$$
$$\left. - \left[\exp\left(-\frac{(1-\alpha)\cdot F \cdot \eta}{R \cdot T}\right) \cdot \left(\frac{-(1-\alpha)\cdot F}{R \cdot T}\right) + \exp\left(\frac{\alpha \cdot F \cdot \eta}{R \cdot T}\right) \cdot \left(\frac{\alpha \cdot F}{R \cdot T}\right)\right] \cdot A\right\} \cdot \frac{1}{B^2} \qquad \text{(A.3)}$$

$$\frac{\partial C^{s}_{V^{2+}}}{\partial C^{b}_{V^{2+}}} = \left\{\frac{D}{r_p \cdot k^{-}} + \exp\left(-\frac{(1-\alpha)\cdot F \cdot \eta}{R \cdot T}\right)\right\} \cdot \frac{1}{B}$$

$$\frac{\partial C^{s}_{V^{2+}}}{\partial C^{b}_{V^{3+}}} = \exp\left(-\frac{(1-\alpha)\cdot F \cdot \eta}{R \cdot T}\right) \cdot \frac{1}{B}$$

- V^{3+} surface concentration:

$$A_1 = C^{s}_{V^{2+}} \cdot \exp\left(\frac{\alpha \cdot F \cdot \eta}{R \cdot T}\right) - \left(C^{b}_{V^{2+}} - C^{s}_{V^{2+}}\right) \cdot \frac{D}{r_p \cdot k^{-}}$$

$$B_1 = \exp\left(-\frac{(1-\alpha)\cdot F \cdot \eta}{R \cdot T}\right)$$

$$\frac{\partial C^{s}_{V^{3+}}}{\partial \eta} = \left\{C^{s}_{V^{2+}} \cdot \exp\left(\frac{\alpha \cdot F \cdot \eta}{R \cdot T}\right) \cdot \left(\frac{\alpha \cdot F}{R \cdot T}\right) \cdot B_1 - \exp\left(-\frac{(1-\alpha)\cdot F \cdot \eta}{R \cdot T}\right) \cdot \left(\frac{-(1-\alpha)\cdot F}{R \cdot T}\right) \cdot A_1\right\} \cdot \frac{1}{B_1^2} \qquad \text{(A.4)}$$

$$\frac{\partial C^{s}_{V^{3+}}}{\partial C^{s}_{V^{2+}}} = \left\{\exp\left(\frac{\alpha \cdot F \cdot \eta}{R \cdot T}\right) + \frac{D}{r_p \cdot k^{-}}\right\} \cdot \frac{1}{B_1}$$

$$\frac{\partial C^{s}_{V^{3+}}}{\partial C^{b}_{V^{2+}}} = -\frac{D}{r_p \cdot k^{-}} \cdot \frac{1}{B_1}$$

Appendix B

Figure B.1 illustrates the comparison between model simulation and experimental data of the first impedance arch at different operating current: the model provides a good fit of the experiments in all the investigated operating conditions.

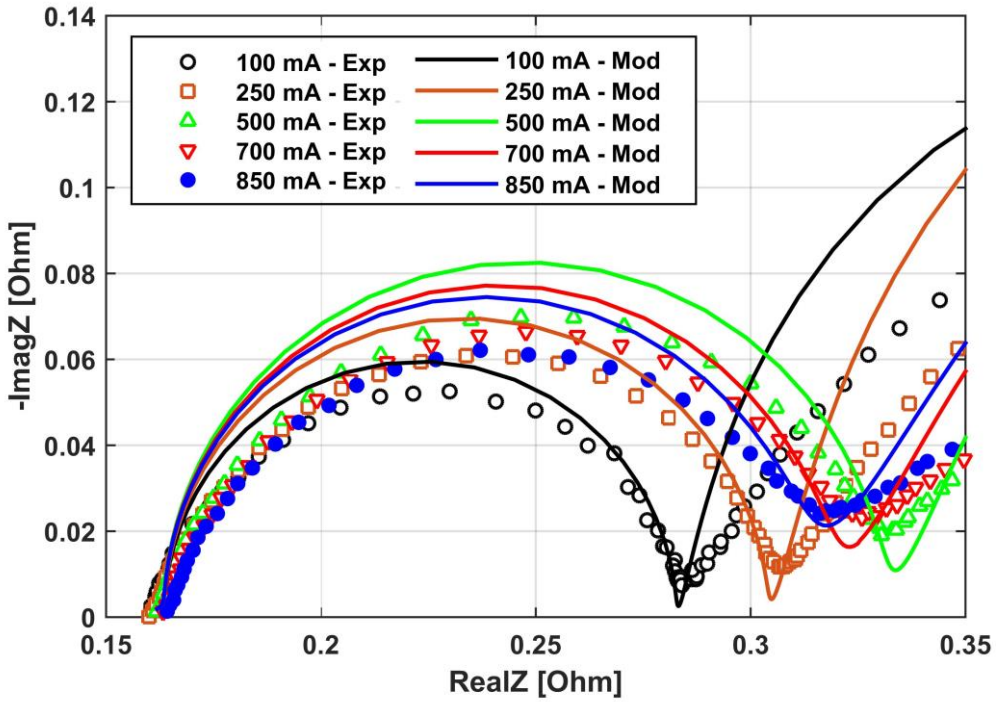

Figure B.1 – Comparison between simulated and measured first arch impedance at 30 ml min^{-1} and 0.8 M.

Appendix C

Figure C.1 illustrates the distribution of V^{2+} concentration through electrode thickness at 100 mA and 850 mA with and without losses related to convection at carbon fiber. At 850 mA the characteristic length of diffusion reduces, resulting in a decreased diffusion resistance compared with the one evaluated at 100 mA (Figure 6).

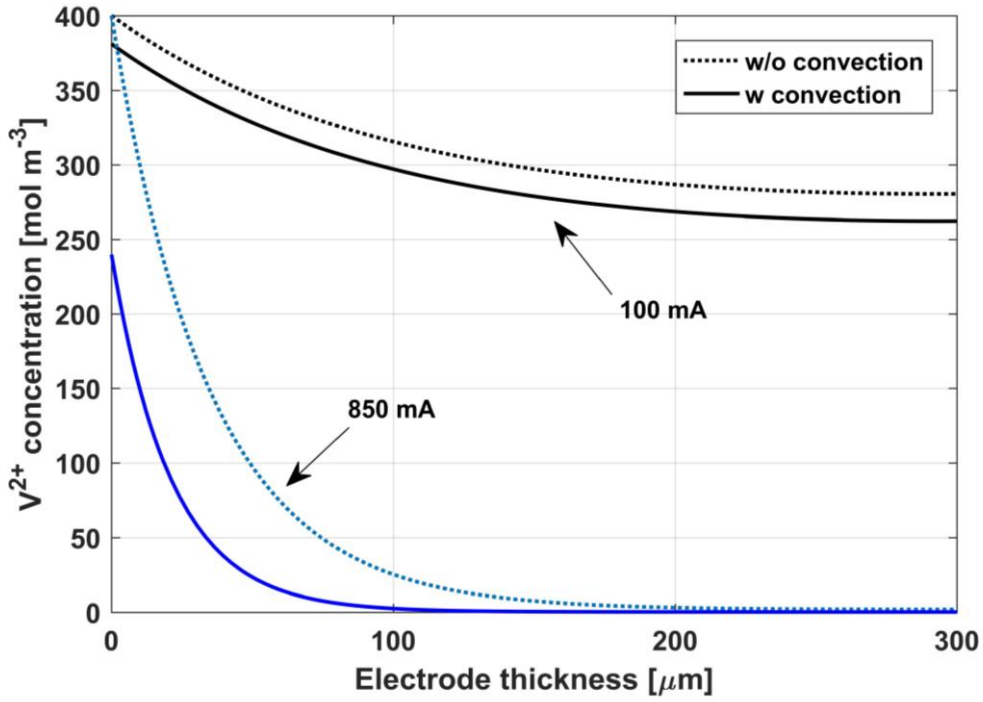

Figure C.1 – V^{2+} concentration through electrode thickness during V^{2+} oxidation with and without losses related to convection at the carbon fiber (zero electrode thickness at channel interface).

Appendix D

Figure D.1 illustrates the calculated resistances and the ionic current profiles through the electrode during V^{2+} oxidation at 320 mA and 0.8 M, elucidating the impact of electrolyte flow rate.

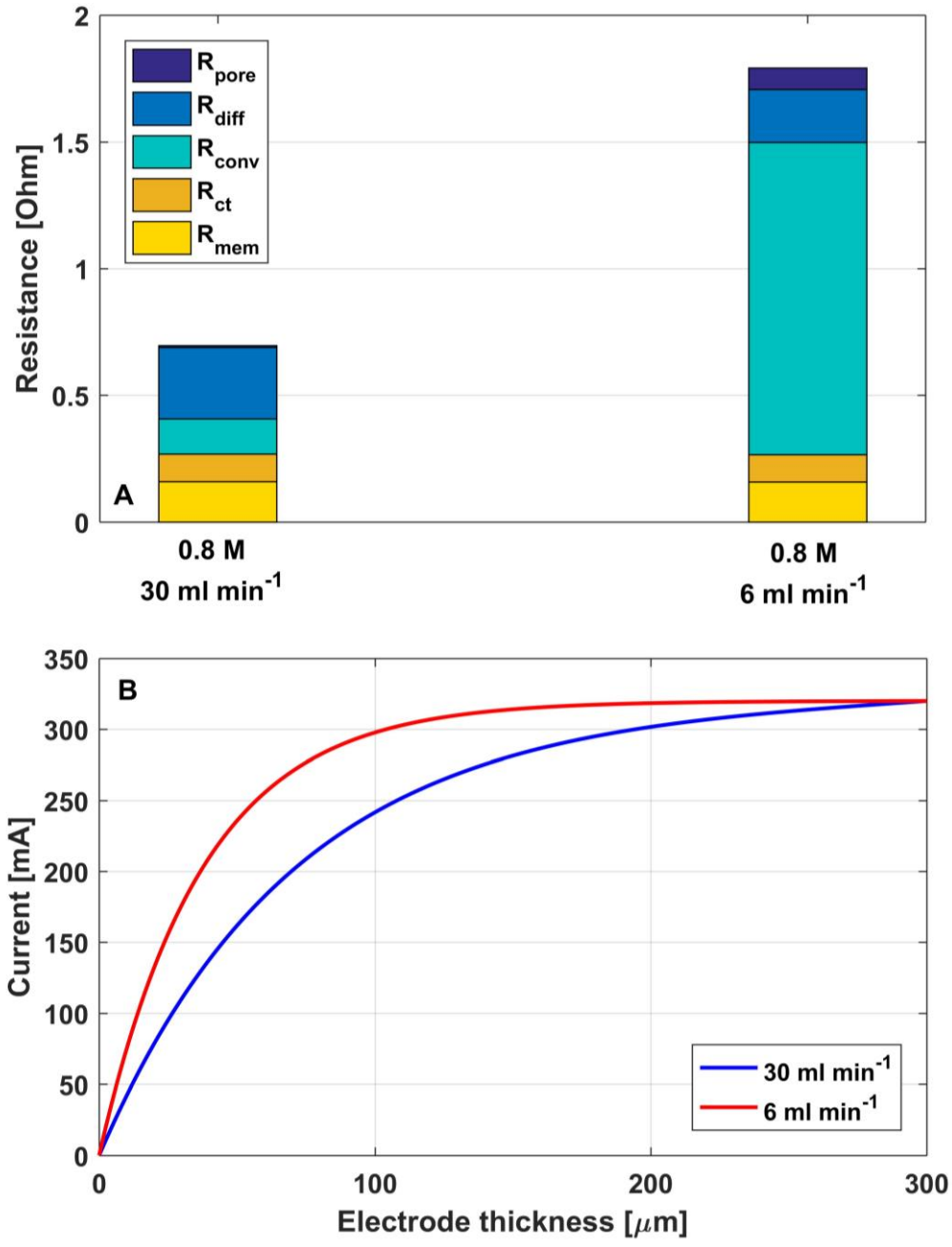

Figure D.1 – Simulations at 320 mA, 0.8 M with 30 ml min^{-1} and 6 ml min^{-1} electrolyte flow rates: A) Comparison between resistances associated to different physical phenomena; B) ionic current distribution through electrode thickness during V^{2+} oxidation (zero electrode thickness at channel interface).

List of symbols

C	Species concentration (mol m^{-3})
N	Species flux (mol s^{-1} m^{-2})
D	Diffusivity (m^2 s^{-1})
D^{eff}	Effective diffusivity (m^2 s^{-1})
r_p	Pore radius (m^{-1})
F	Faraday constant (C mol^{-1})
R	Universal gas constant (J mol^{-1} K^{-1})
T	Temperature (K)
E_0	Standard equilibrium potential (V)
i_v	Volumetric reaction current density (A m^{-3})
i	Current density (A m^{-2})
k-	Rate constant (m s^{-1})
a	Specific surface area (m^{-1})
l	Thickness (m)
z	Species valence (-)
x	x coordinate (m)
t	time (s)
C_{dl}	Double layer capacitance (F m^{-3})
Z	Impedance (Ω or Ω cm^2)
R_{mem}	Resistance associated to membrane loss (Ω)
R_{ct}	Resistance associated to charge transfer loss (Ω)
R_{conv}	Resistance associated to convection loss (Ω)
R_{pore}	Resistance associated to loss in the pore (Ω)
R_{diff}	Resistance associated to diffusion loss (Ω)
R_{mig}	Resistance associated to migration loss (Ω)

Greek symbol

ΔV	Cell potential difference (V)
ε_{el}	Electrode porosity (-)
α	Transfer coefficient (-)
η	Electrode polarization (V)
ϕ	Potential (V)
η_{Ohm}	Membrane overpotential (V)
ω	Angular frequency (rad s^{-1})
σ_s	Catalyst layer electronic conductivity (Ω^{-1} m^{-1})
σ_m	Membrane ionic conductivity (Ω^{-1} m^{-1})

Superscript

b	Relative to bulk
s	Relative to surface
ch	Relative to channel
in	Relative to inlet
~	Relative to oscillating quantity

Subscript

s	Relative to solid phase
l	Relative to liquid phase
ox	Relative to oxidation
rd	Relative to reduction
m	Relative to membrane
el	Relative to electrode
ch-el	Relative to channel-electrode interface

el-m	Relative to electrode-membrane interface
0	Relative to steady-state
V^{2+}	Relative to Vanadium II ion
V^{3+}	Relative to Vanadium III ion
H^{+}	Relative to proton
HSO_4^-	Relative to hydrogen sulfate ion
SO_4^{2-}	Relative to sulfate ion

Bibliography

[1] P. Alotto, M. Guarnieri, F. Moro, Redox flow batteries for the storage of renewable energy: a review, Renewable and Sustainable Energy Reviews 29 (2014) 325-335.

[2] G.L. Soloveichik, Flow batteries: current status and trends, Chemical Reviews 115 (2015) 11533–11558.

[3] A. Parasuraman, T.M. Lim, C. Menictas, M. Skyllas-Kazacos, Review of material research and development for vanadium redox flow battery applications, Electrochimica Acta 101 (2013) 27–40.

[4] A.Z. Weber, M.M. Mench, J.P. Meyers, P.N. Ross, J.T. Gostick, Q. Liu, Redox flow batteries: a review, Journal of Applied Electrochemistry 41 (2011) 1137–1164.

[5] M. Wu, M. Liu, G. Long, K. Wan, Z. Liang, T.S. Zhao, A novel high-energy-density positive electrolyte with multiple redox couples for redox flow batteries, Applied Energy 136 (2014) 576–581.

[6] M.H. Chakrabarti, N.P. Brandon, S.A. Hajimolana, F. Tariq, V. Yufit, M.A. Hashim, M.A. Hussain, C.T.J. Low, P.V. Aravind, Application of carbon materials in redox flow batteries, Journal of Power Sources 253 (2014) 150-166.

[7] B. Zakeri, S. Syri, Electrical energy storage systems: a comparative life cycle cost analysis, Renewable and Sustainable Energy Reviews 42 (2015) 569–596.

[8] Y.K. Zeng, T.S. Zhao, L. An, X.L. Zhou, L. Wei, A comparative study of all-vanadium and iron-chromium redox flow batteries for large-scale energy storage, Journal of Power Sources 300 (2015) 438-443.

[9] J. Houser, J. Clement, A. Pezeshki, M.M. Mench, Influence of architecture and material properties on vanadium redox flow battery performance, Journal of Power Sources 302 (2016) 369-377.

[10] Q. Xu, T.S. Zhao, P.K. Leung, Numerical investigations of flow field designs for vanadium redox flow batteries, Applied Energy 105 (2013) 47–56.

[11] X. Ke, J.I.D. Alexander, J.M. Prahl, R.F. Savinell, Flow distribution and maximum current density studies in redox flow batteries with a single passage of the serpentine flow channel, Journal of Power Sources 270 (2014) 646-657.

[12] E. Barsoukov, J.R. Macdonald, Impedance spectroscopy, theory, experiment, and applications, second edition, Wiley-Interscience, New York, 2005.

[13] A. Baricci, M. Zago, A. Casalegno, Modelling analysis of heterogeneity of ageing in high temperature polymer electrolyte fuel cells: insight into the evolution of electrochemical impedance spectra, Electrochimica Acta 222 (2016) 596–607.

[14] A.A. Kulikovsky, A physical model for catalyst layer impedance, Journal of Electroanalytical Chemistry (2012), 669, 28–34.

[15] B.P. Setzler, T.F. Fuller, A physics-based impedance model of proton exchange membrane fuel cells exhibiting low-frequency inductive loops, Journal of The Electrochemical Society 162 (2015) F519-F530.

[16] M. Zago, A. Casalegno, A physical model of direct methanol fuel cell anode impedance, Journal of Power Sources (2014), 248, 1181-1190.

[17] A. Baricci, M. Zago, A. Casalegno, A quasi 2D model of a high temperature polymer fuel cell for the interpretation of impedance spectra, Fuel Cells (2014), 14, 926-937.

[18] T.E. Springer, T.A. Zawodzinski, M.S. Wilson, S. Gottesfeld, Characterization of polymer electrolyte fuel cells using AC impedance spectroscopy, Journal of The Electrochemical Society 143 (1996) 587-599.

[19] W.G. Bessler, A new computational approach for SOFC impedance from detailed electrochemical reaction–diffusion models, Solid State Ionics 176 (2005) 997-1011,

[20] W.G. Bessler, S. Gewies, M. Vogler, A new framework for physically based modeling of solid oxide fuel cells, Electrochimica Acta 53 (2007) 1782-1800.

[21] H. Fink, J. Friedl, U. Stimming, Composition of the electrode determines which half- cell's rate constant is higher in a vanadium flow battery, The Journal of Physical Chemistry C 120 (2016) 15893–15901.

[22] J. Friedl, C.M. Bauer, A. Rinaldi, U. Stimming, Electron transfer kinetics of the VO^{2+}/VO^{+}_{2} – Reaction on multi-walled carbon nanotubes, Carbon 63 (2013) 228-239.

[23] C.N. Sun, F.M. Delnick, D.S. Aaron, A.B. Papandrew, M.M. Mench, T.A. Zawodzinski, Resolving losses at the negative electrode in All-Vanadium Redox Flow Batteries using electrochemical impedance spectroscopy, Journal of The Electrochemical Society 161 (2014) A981-A988.

[24] G. Paasch, K. Micka, P. Gersdorf, Theory of the electrochemical impedance of macrohomogeneous porous electrodes, Electrochimica Acta 38 (1993) 2653-2662.

[25] A.M. Pezeshki, R.L. Sacci, F.M. Delnick, D.S. Aaron, M.M. Mench, Elucidating effects of cell architecture, electrode material, and solution composition on overpotentials in redox flow batteries, Electrochimica Acta 229 (2017) 261-270.

[26] C.N. Sun, F.M. Delnick, D.S. Aaron, A.B. Papandrew, M.M. Mench, T.A. Zawodzinski, Probing electrode losses in all-Vanadium Redox Flow Batteries with impedance spectroscopy, ECS Electrochemistry Letters, 2 (2013) A43-A45.

[27] R.M. Darling, M.L. Perry, Half-cell, steady-state flow-battery experiments, ECS Transactions 53 (2013) 31-38.

[28] K.W. Knehr, E. Agar, C.R. Dennison, A.R. Kalidindi, E.C. Kumbur, A transient vanadium flow battery model incorporating vanadium crossover and water transport through the membrane, Journal of The Electrochemical Society (2012), 159, A1446-A1459.

[29] J.T. Clement, D.S. Aaron, M.M. Mench, In situ localized current distribution measurements in all-Vanadium Redox Flow Batteries, Journal of The Electrochemical Society 163 (2016) A5220-A5228.

[30] A.A. Shah, M.J. Watt-Smith, F.C. Walsh, A dynamic performance model for redox-flow batteries involving soluble species, Electrochimica Acta 53 (2008) 8087-8100.

[31] A.J. Bard, L.R. Faulkner, Electrochemical methods, fundamentals and applications, second edition, Wiley, New York, 2001.

[32] C.L. Chen, H.K. Yeoh, M.H. Chakrabarti, An enhancement to Vynnycky's model for the all-vanadium redox flow battery, Electrochimica Acta (2014), 120, 167–179.

[33] D. Schmal, J. Van Erkel, P.J. Van Duin, Mass transfer at carbon fibre electrodes, Journal of Applied Electrochemistry 16 (1986) 442-430.

[34] R.H. Perry, D.W. Green, Perry's Chemical Engineer's Handbook, McGraw-Hill, 1999.

[35] M.E. Orazem, B. Tribollet, Electrochemical Impedance Spectroscopy, Wiley, New York, 2008.

[36] S. Gewies, W.G. Bessler, Physically based impedance modeling of Ni/YSZ cermet anodes, Journal of The Electrochemical Society 155 (2008) B937-B952.

[37] A. Parthasarathy, B. Davé, S. Srinivasan, A.J. Appleby, C.R. Martin, The platinum microelectrode/nafion interface: an electrochemical impedance spectroscopic analysis of oxygen reduction kinetics and nafion characteristics, Journal of The Electrochemical Society 139 (1992) 1634-1641.

List of tables

Table 1 –Investigated operating conditions.

	Condition 1	Condition 2	Condition 3
Flow rate [ml min^{-1}]	30	30	6
Vanadium concentration [M]	0,8	0,1	0,8
State of Charge [%]	50	50	50
Minimum stoichiometry [-]	22 (@ 850 mA)	13 (@ 190 mA)	12 (@320 mA)

Table 2 – Assumed and fitted model parameters.

Symbol	Value	Unit	
A_{cell}	5×10^{-4}	[m^2]	assumed
l_m	1.83×10^{-4}	[m]	assumed
l_{el}	3×10^{-4}	[m]	assumed
ε_{el}	0,9	[-]	assumed
D_{V2+}	1.8×10^{-9}	[m^2 s^{-1}]	fitted
D_{V3+}	1.8×10^{-9}	[m^2 s^{-1}]	fitted
D_{H+}	9.3×10^{-9}	[m^2 s^{-1}]	[28]
D_{SO42-}	1.1×10^{-9}	[m^2 s^{-1}]	[28]
D_{HSO4-}	1.3×10^{-9}	[m^2 s^{-1}]	[28]
h_{conv} at 30 ml min^{-1}	1.1×10^{-4}	[m s^{-1}]	fitted
h_{conv} at 6 ml min^{-1}	2.75×10^{-5}	[m s^{-1}]	fitted
E_0	-0,255	[V]	[28]
α	0,46	[-]	fitted
k^-	2.24×10^{-6}	[m s^{-1}]	fitted
a	3.5×10^4	[m^{-1}]	[28]
σ_s	1000	[S m^{-1}]	[28]
σ_m at 0.8 M	2,3	[S m^{-1}]	fitted
σ_m at 0.1 M	3,2	[S m^{-1}]	fitted
r_p	2.4×10^{-6}	[m]	assumed
ρ_l	1300	[kg m^{-3}]	[28]
C_{dl}	3.2×10^4	F m^{-3}	fitted